



Triblock polymer mediated synthesis of Ir–Sn oxide electrocatalysts for oxygen evolution reaction

Guangfu Li^{a,b}, Hongmei Yu^{a,*}, Xunying Wang^{a,b}, Donglei Yang^{a,b}, Yongkun Li^{a,b}, Zhigang Shao^a, Baolian Yi^a

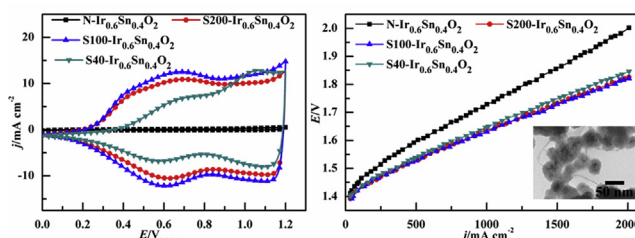
^a Laboratory of Fuel Cells, Dalian Institute of Chemical Physics, Chinese Academy of Sciences, 457 Zhongshan Road, Dalian 116023, PR China

^b Graduate School of the Chinese Academy of Sciences, Beijing 100039, PR China

HIGHLIGHTS

- Ir–Sn oxide is synthesized by an advanced soft-material assistant method.
- Ir–Sn oxide properties depend on the F127 content.
- Ir–Sn oxide shows significantly high activity and stability for O₂ evolution.
- The noble-metal loading in the water electrolysis anode is only 0.77 mg cm^{−2}.

GRAPHICAL ABSTRACT



ARTICLE INFO

Article history:

Received 7 July 2013

Received in revised form

18 October 2013

Accepted 21 October 2013

Available online 30 October 2013

Keywords:

Low noble-metal loading

Iridium–tin oxide electrocatalyst

Oxygen evolution reaction

Proton exchange membrane water

electrolyzer

Triblock polymer surfactant

ABSTRACT

Over the past several decades, tremendous effort has been put into developing cost-effective, highly active and durable electrocatalysts for oxygen evolution reaction (OER) in the proton exchange membrane water electrolyzer. This report explores an advanced and effective “soft” material-assistant method to fabricate Ir_{0.6}Sn_{0.4}O₂ electrocatalysts with a 0.6/0.4 ratio of Ir/Sn in precursors. Adopting a series of characterization methods, the collective results suggest that the surfactant–material F127 content, as an important factor, can efficiently control the formation of Ir–Sn oxides with varying surface properties and morphologies, such as the grainy and rod-shaped structures. Associating with the half-cell and single electrolyzer, it is affirmed that the optimal ratio of (Ir + Sn)/F127 is 100 for the preparation of S100-Ir_{0.6}Sn_{0.4}O₂ with obviously enhanced activity and sufficient durability under the electrolysis circumstances. The lowest cell voltages obtained at 80 °C are 1.631 V at 1000 mA cm^{−2}, and 1.820 V at 2000 mA cm^{−2}, when applying S100-Ir_{0.6}Sn_{0.4}O₂ OER catalyst and Ti-material diffusion layer on the anode side and Nafion® 115 membrane. Furthermore, the noble-metal Ir loading in the same cell decreases to 0.77 mg cm^{−2}. These results highlight that Ir–Sn oxide synthesized by the soft-material method is a promising OER electrocatalyst.

© 2013 Published by Elsevier B.V.

1. Introduction

H₂ generation by water electrolysis (WE) has received increasing attention as an alternative technology for energy conversion and storage [1–3]. In alkaline medium, non-precious metals can be employed as electrocatalysts because of the lower equilibrium potentials both on the cathode and anode electrodes at the high pH

(over 13 in general) [4–8]. However, the alkaline electrolyte has relatively low ion conductivity and is susceptible to the formation of carbonate as a contaminant by the reaction with CO₂ [9]. In contrast, using proton exchange membrane (PEM) electrolyzer architectures, the electrochemical process in the acid medium makes it possible to produce considerably higher operational current density, though precious metals are required for the oxygen evolution reaction (OER) [9–11]. Due to the slower kinetics, higher overpotential for OER in the anode than the hydrogen-evolution process in the cathode, more effort has been devoted to the

* Corresponding author. Tel.: +86 411 84379051; fax: +86 411 84379185.

E-mail address: hmyu@dicp.ac.cn (H. Yu).

development of a high active, long-term stable and inexpensive electrocatalyst for OER [10–19].

As a matter of fact, it has been well accepted that IrO_2 with the superior electrochemical stability and activity has emerged as the most promising catalyst candidate for OER in the strong acidic electrolyte, and therefore is frequently reported [14,18,20–24]. Recent research has focused on the reduction of the noble-metal loading in PEM water electrolysis (PEMWE) cells, e.g. by preparing mesoporous metal oxide films [14,20] and multi-component catalysts. Multi-component electrocatalysts containing Ir are usually prepared with the combination of one or more less-expensive metal oxides, such as TiO_2 [25,26], TiC [27], SnO_2 [15,28,29], Sb_2O_5 – SnO_2 [30,31], Ta_2O_5 [32], etc., the activity and durability of which are determined by numerous factors. Nevertheless the effective control of the design and synthesis of these catalysts is still quite difficult to achieve by adopting some traditional synthetic routes, including Adams-fusion and colloidal methods [11,19]. As a matter of fact, the catalytic properties of a multi-component material depend not only on the chemical nature of the components and their ratio but also on the crystal phase, surface properties and even its nano- or micro-morphology, all of which strongly influenced by the preparation approach. In our previous work, the morphology-controlled IrO_2 and IrO_2 – RuO_2 synthesized using the zeolite hard-template method has showed some obvious advantages toward OER, compared with those with the traditional Adams-fusion method [21,33].

On the other hand, solution phase synthesis for the nano-structures also revolved with a soft material or surfactant that achieves fine control over the size and shape of the catalysts [34–37], but it was still scarce to utilize the soft material to synthesize IrO_2 -based electrocatalysts in the published researches. Triblock polymers (TBPs) with repeating units of polyethylene oxide (PEO) and polypropylene oxide (PPO) have a promising application to direct metal/oxide nanoparticle (NP) synthesis. Their unique and attractive features are referred to the commercial availability and biocompatibility, and thus result in a methodology with affordable cost and low impact to the environment [35]. It has been discovered that TBPs can act as efficient stabilizers, structure-directing agents and mild reductants, and correspondingly can control finely NP morphology and organization [35,38]. However, the TBP-assistant approach should be developed to prepare the IrO_2 -based oxide powder with highly desirable performance toward OER.

The present study reports the innovative synthesis of the $\text{Ir}_{0.6}\text{Sn}_{0.4}\text{O}_2$ electrocatalysts with the same molar ratio of Ir/Sn (0.6/0.4) in metal-precursor solutions employing a TBP-assistant method. The commercial PEO–PPO–PEO Pluronic® F127 was selected as the soft polymer material, due to its unique structure, appropriate polymer length and highly thermodynamic stability. Employing a wide range of physicochemical characterization techniques, the collective data confirmed that the $\text{Ir}_{0.6}\text{Sn}_{0.4}\text{O}_2$ samples with flexible structures were produced only by the changed TBP content. The half-cell and electrolyzer tests revealed that the soft-material route highlighted the promising potential of the Ir–Sn oxide electrocatalyst for OER with remarkable activity and stability, and low noble-metal loading.

2. Experimental

2.1. Materials and reagents

Sodium borohydride (NaBH_4 , $\geq 96\%$), anhydrous ethanol (95–98%), isopropanol, anhydrous stannic chloride (SnCl_4 , $\geq 99\%$), hydrochloric acid (HCl , 36–38%), hydrogen peroxide (H_2O_2 , $\geq 30\%$) and sulfuric acid (H_2SO_4 , 95–98%) were purchased from Tianjin Chemical Reagent Company. Hexachloroiridium acid hydrate ($\text{H}_2\text{IrCl}_6 \cdot x\text{H}_2\text{O}$, 35% in Ir) was obtained from Shanghai July Chemical

Company. TBP Pluronic® F127 (PEO_{100} – PPO_{65} – PEO_{100}) were supplied by Sigma–Aldrich. Commercial Pt/C (70% in Pt) was purchased from Johnson Matthey. Nafion® solution (5%) and Nafion® 115 membrane were obtained from Dupont. All chemicals were reagent grade and were used without further purification.

2.2. Preparation of Ir–Sn oxides

We attempted to optimize the F127 amount in order to control the Ir–Sn oxide synthesis. In a typical experimental to synthesize $\text{Ir}_{0.6}\text{Sn}_{0.4}\text{O}_2$ samples with the same molar ratio of Ir/Sn (0.6/0.4) in precursors, the varied amounts of F127 were dissolved in 60.8 mL of deionized water, and the resulting solution was then stirred at 60 °C for 0.5 h. The metal-precursor solutions containing H_2IrCl_6 and SnCl_4 were injected into the TBP solution, and 0.02 M of total metal concentration was achieved. After vigorously stirring overnight, the mixture solution was sequentially added dropwise in a 1 M of NaBH_4 solution (12.2 mL) with the same F127 content in order to avoid formation of F127 concentration gradient existing between the reductant solution and metal precursor solutions. The resulting solution bubbled furiously and changed within 15 min to brown, then to navy blue quickly, indicating the successful reduction of Ir. The reaction was allowed to proceed at 60 °C for 12 h under continuous stirring, and aged at room temperature under static condition overnight. The resulting product was collected by centrifugation at 9500 rpm for 8 min and large amounts of F127 were removed by 4–5 consecutive washing/centrifugation cycles with anhydrous ethanol. Followed by drying at 40 °C, the as-synthesized Ir–Sn sample was then calcined in air at 400 °C for 2 h in order to remove the residual surfactant and to promote Ir–Sn oxide alloy formation. In this work, x -value of $\text{Sx-Ir}_{0.6}\text{Sn}_{0.4}\text{O}_2$ ($x = 200, 100$ and 40) was defined by the following equation:

$$x = (n_{\text{Ir}} + n_{\text{Sn}})/n_{\text{F127}} \quad (1)$$

where n is the feeding molar content of the various materials. For comparison, the $\text{N-Ir}_{0.6}\text{Sn}_{0.4}\text{O}_2$ sample without F127 was also prepared by employing the similar procedure.

2.3. Physicochemical characterization

TEM (JEM-2000EX) images were recorded with an accelerated voltage of 120 kV. ICP analysis for Ir and Sn metals was performed by Shimadzu (JPN.) ICPS-8100 after digestion of power samples in HCl and H_2O_2 . Powder XRD measurements were carried out by using an X'Pert Pro Diffractometer (PAN-alytical) with a $\text{CuK}\alpha$ tube at 40 kV and 40 mA. The physical surface area and total pore volume were determined by N_2 absorption/desorption measurements with a Quantachrome Autosorb-1-C at 77 K. Prior to adsorption, all samples were degassed in vacuum at 200 °C for 2 h. Brunauer–Emmett–Teller (BET) formulation and Barrett–Joyner–Halenda (BJH) mode were utilized to estimate the surface area and total pore volume, respectively. In order to analyze the surface composition of catalysts, X-ray photoelectron spectroscopy (XPS, ESCALAB 250Xi) was performed with a monochromatic Mg radiation. The hydrocarbon C1s signal at 284.6 eV was used as the energy reference for calibration [39,40]. The XPS spectra were fitted using XPSPEAK software with a Gaussian–Lorentzian product function and a non-linear Shirley background.

2.4. Half-cell tests

Both the activity and stability of the prepared Ir–Sn catalysts toward OER were characterized by half-cell tests, i.e., cyclic voltammetry (CV) and linear sweep voltammetry (LSV), which were

conducted on a CHI 630C electrochemical workstation (CH Instruments) in N₂-purged 0.5 M H₂SO₄ at room temperature. Measurements were carried out in a conventional three-electrode system, which was composed of a glassy carbon electrode (GCE, 4 mm in diameter) with a thin layer of electrocatalyst as the working electrode, a Pt foil counter electrode and a saturated calomel electrode (SCE) reference electrode. A thin layer of catalyst was deposited on GCE as follows: a mixture including 1 mL of ethanol, 5.0 mg of home-made catalyst and 50 μ L of Nafion[®] solution (5%) was homogenized for 45 min in an ultrasonic bath. The ink (25 μ L) was then drop casted on the prepolished GCE surface and dried in air.

The scan potential window of CV was from 0 to 1.2 V_{SCE}, and the scan rate ranged from 2 to 300 mV s⁻¹. The charge (*Q*) was calculated from the different voltammograms at various scan rates, by the following equation:

$$Q = \int_{E_1}^{E_2} \frac{|j|}{m_{Ir} \nu} dE \quad (2)$$

where *j* is the current density obtained in CV curves, ν is the scan rate ranged from 2 to 300 mV s⁻¹, and *E* is the scan potential between 0.15 and 1.15 V_{SCE}. The LSV tests were performed from 1.15 to 1.4 V_{SCE} at a scan rate of 2 mV s⁻¹. The electrolyte was deoxygenated via bubbling N₂ for 30 min prior and during all measurements.

2.5. PEMWE cell tests

The single cell properties of electrocatalysts were evaluated in a home-made PEMWE cell with an active area of 5 cm² [33]. Nafion[®] 115 membrane (ca. 127 μ m thickness) was chosen as the solid polymer electrolyte. Prior to electrodes preparation, membranes were pretreated as described in our previous reports [21,33]. To prepare a thin catalyst coated membrane (CCM) electrode with a sandwich-like structure, 5 wt% of Nafion[®] solution (0.6 mg cm⁻²) and isopropanol were sprayed onto each side of membrane, followed by spraying electrocatalyst and Nafion[®] solution (1/3 of the mass of catalyst). The catalyst loadings obtained by weighing were 70 wt% Pt/C (0.4 mg cm⁻² of Pt) in the cathode and 1.5 mg cm⁻² of Ir_{0.6}Sn_{0.4}O₂ in the anode. A Pt-plated porous Ti (7 μ m thickness) and wet-proof carbon paper were used as the anode and cathode diffusion layers, respectively. The membrane electrode assembly (MEA) was fabricated by hot pressing the prepared CCM and cathode diffusion layer at 120 °C and 0.1 MPa for 1 min.

Electrochemical impedance spectroscopy (EIS) data were obtained at 1.45 V with an alternated signal of 10 mV on Solartron[®] 1287 Electrochemical Interface in conjunction with Solartron[®] 1260 Frequency Response Analyzer. Sweeping frequency range was between 0.1 Hz and 10 kHz. The impedance diagrams were analyzed and modeled using the ZView program of Solartron, version 3.0. Steady state polarization tests were conducted at 80 °C and atmospheric pressure in potentiostatic mode. To perform PEM water electrolysis, deionized water as the reactant of was provided to anode compartments at 50 mL min⁻¹.

3. Results and discussion

3.1. Physicochemical characteristics

Morphology features of the synthesized samples were analyzed by TEM. Fig. 1a shows the TEM image of as-synthesized S100-Ir_{0.6}Sn_{0.4}O₂ NPs organized by F127 micellar assemblies. It was a good proof that the Ir–Sn NPs could be completely wrapped and/or positioned by the TBP micelles with the spheric-like structure (ca.

24.4 nm in diameter), and in the nanomicelle reactors, was effectively protected from particle aggregation. For the 400 °C calcined S100-Ir_{0.6}Sn_{0.4}O₂ specimen (Fig. 1b), the particles were observed with slight aggregation and sinter, owing to the removal of residual TBP, crystallization and oxidation of Ir–Sn metal species in the calcination treatment process, and the average particle size was around 10.6 nm. With the increase of the TBP F127 content, the catalyst structure revealed the grain-to-rod transition. As shown in Fig. 1c, the S40-Ir_{0.6}Sn_{0.4}O₂ sample prepared using the molar ratio of (Ir + Sn)/F127 = 40 in precursors was observed with (ca.) 6.8 nm of mean rod diameter. According to Landazuri and coworkers [41], it exhibited a steady growth as rods throughout the increased content, and the origin of the grain-to-rod transition may be related to the size of the spherical aggregates. The TEM image (Fig. 1d) of N-Ir_{0.6}Sn_{0.4}O₂ synthesized without F127 presented many fine rod structure with around 4.5 nm diameter.

The synthesized *x*-Ir_{0.6}Sn_{0.4}O₂ (*x* = S100, S40 and N) samples were chosen for further HRTEM analysis. Fig. 2a shows the initial images obtained from the S100-Ir_{0.6}Sn_{0.4}O₂ nanoparticles. The large numbers of lattice fringes were not observed especially at the edge of particles, suggesting the formation of the amorphous structure. Whereas, after exposure in electron beam for over 5 min at an accelerated voltage of 300 kV (Fig. 2b), the fringes of S100-Ir_{0.6}Sn_{0.4}O₂ could be clearly detected and the amorphous oxide turned to a highly crystal line phase. The distances between the neighboring lattice fringes (*d*-spacing) were approximately 0.23 nm, which corresponds to the (1 0 1) planes of the rutile oxide phase. From the images of the synthesized S40- and N-Ir_{0.6}Sn_{0.4}O₂ nanorods, these materials appeared to be high crystalline, as evidenced by its clean lattice fringes (Fig. 2c and d). The interplanar separations between the lattice fringes are around 0.32 nm, with the lattice fringes on the (1 1 0) planes of the rutile structure.

The Ir molar content of all the synthetic samples was 0.6 in precursors; while in the prepared bulk measured by ICP (Table 1) was around 0.5, resulting from the partial reduction of the Ir precursor. In other words, it means that the reductive Ir NPs were oxidized partly in air and then dissolved into solution. In our early study, it is found that the metal particles were prone to serious agglomeration, and correspondingly resulting in poor performance for OER, when the metal species was more sufficiently reduced by increasing the reaction temperature or the content of the NaBH₄ reductant solution. On the other hand, the Ir content of the TBP-assistant S200- and S100-Ir_{0.6}Sn_{0.4}O₂ was slightly higher than that of the S40- and N-Ir_{0.6}Sn_{0.4}O₂ specimens, which indicated that F127 with a proper content could act as a good protector for Ir species from oxidation.

According to the N₂ adsorption/desorption isotherms for all calcined samples, the specific surface areas and total pore volume were calculated by the BET and BJH, respectively, and results were given in Table 1. The BET surface areas were 65–100 m² g⁻¹ and the total pore volume ranged from 0.34 to 0.78 m³ g⁻¹ for the studied samples, which confirmed that surfactant F127 took a critical function to direct the synthesis of the Ir–Sn oxides with different pore structures. Compared with N-Ir_{0.6}Sn_{0.4}O₂, the increased surface area of S200-Ir_{0.6}Sn_{0.4}O₂ resulted from the F127 protector from metal particle agglomeration. Then the increased F127 content contributed to the Ir–Sn absorption and stabilization, resulting in the decreased surface area, e.g. S100-Ir_{0.6}Sn_{0.4}O₂. Meanwhile, the increased surface area with the further enhanced TBP content could be attributed to the improved dispersion of particles organized by the nanorod-structure TBP micelles, and the increased porosity of S40-Ir_{0.6}Sn_{0.4}O₂ was also detected. The trend of total pore volume with the changed F127 was coincided with the surface area results, and the pore volume for the three TBP-assisted oxides was over double that of N-Ir_{0.6}Sn_{0.4}O₂.

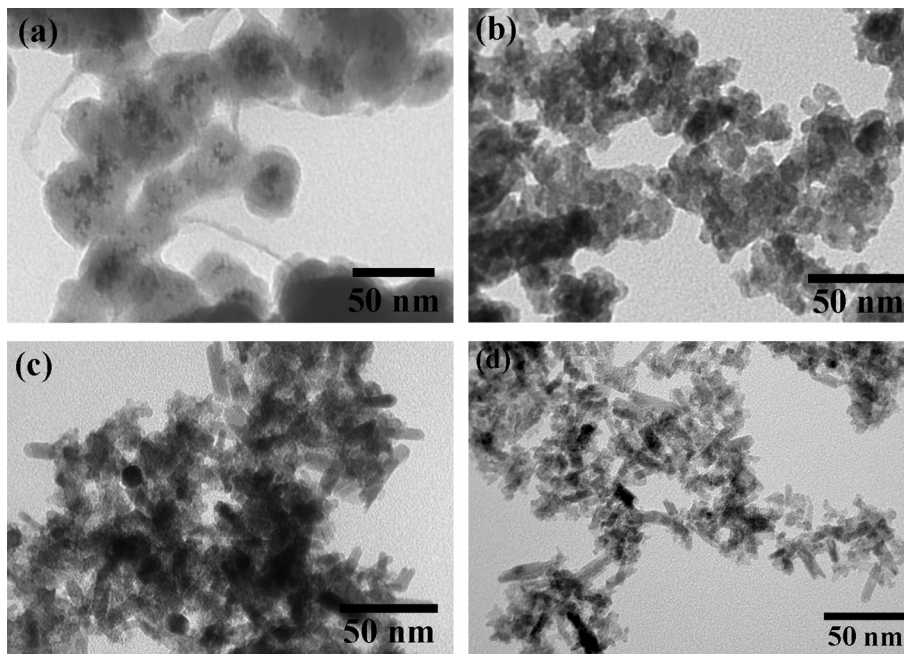


Fig. 1. TEM images of (a) as-synthetic S100-Ir_{0.6}Sn_{0.4}O₂, (b) S100-Ir_{0.6}Sn_{0.4}O₂, (c) S40-Ir_{0.6}Sn_{0.4}O₂ and (d) N-Ir_{0.6}Sn_{0.4}O₂.

The wide angle XRD patterns for the prepared power samples are shown in Fig. 3. According to the main diffracted peaks in the Joint Committee on Powder Diffraction Standards (JCPDS) cards of the rutile IrO₂ (JCPDS:01-088-0288) and SnO₂ (JCPDS:00-041-1445), the synthetic oxides matched a rutile-structure in the whole studied range of the F127 content, and no special peak of Ir and/or Sn metal state was observed. It was also observed in S200- and S100-Ir_{0.6}Sn_{0.4}O₂, that no individual (1 1 0) and (1 0 1) peaks of IrO₂/SnO₂ were discernible at around 27° and 34°, respectively. It demonstrated that these samples formed the amorphous and solid-solution states which provides the large density unsaturated sites

and structural flexibility, and correspondingly improve the OER catalytic performance [42]. The patterns of N- and S40-Ir_{0.6}Sn_{0.4}O₂ were observed with high crystallinity, which would become a consequence of the increased crystallite size and separated Ir and Sn phases, including a Sn-rich phase and an Ir-rich phase. We concluded that it would be difficult for the slender nanorod structure (especially N-Ir_{0.6}Sn_{0.4}O₂) to completely cover the inert SnO₂ sites by the active Ir species, as a response of the increased opportunities of Sn exposedness. Besides, the most outstanding peaks observed in an individual XRD pattern were in respect to the (1 0 1) plane for S100-Ir_{0.6}Sn_{0.4}O₂ and the (1 1 0) plane for S40- and

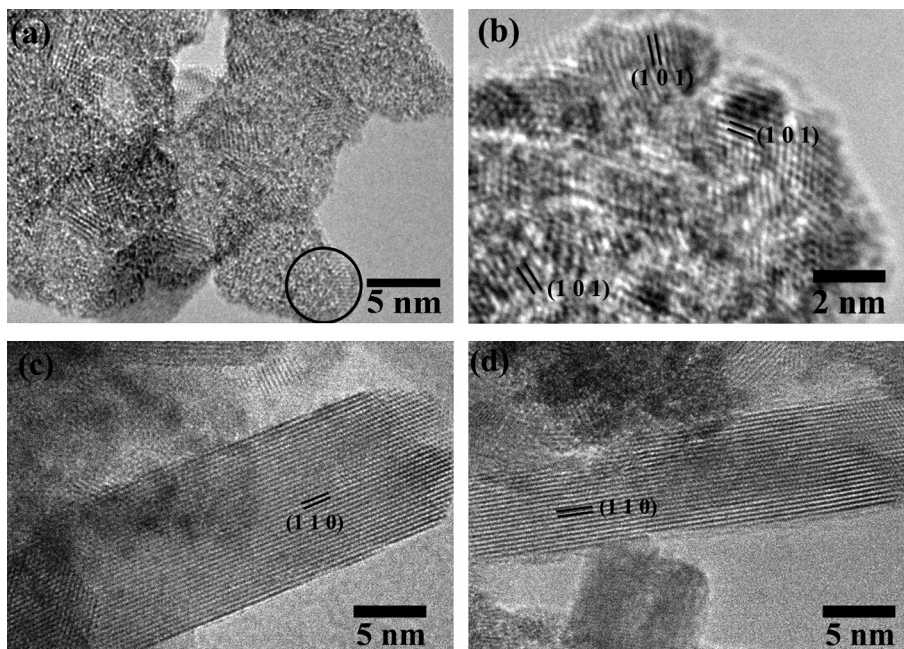


Fig. 2. HRTEM images of (a) S100-Ir_{0.6}Sn_{0.4}O₂, (b) S100-Ir_{0.6}Sn_{0.4}O₂ at a higher magnification after exposing the electron beam for over 5 min at an accelerated voltage of 300 kV, (c) S100-Ir_{0.6}Sn_{0.4}O₂ and (d) N-Ir_{0.6}Sn_{0.4}O₂.

Table 1
Physical properties of various catalyst samples.

Sample	Particle size (nm)	Crystalline size (nm)	Ir/(Ir + Sn) (by ICP)	Surface area (m ² g ⁻¹)	Total pore volume (cm ³ g ⁻¹)
N-Ir _{0.6} Sn _{0.4} O ₂	4.5	4.6	0.449	78.5	0.338
S200-Ir _{0.6} Sn _{0.4} O ₂	—	2.3	0.501	97.1	0.757
S100-Ir _{0.6} Sn _{0.4} O ₂	10.6	2.3	0.500	65.1	0.596
S40-Ir _{0.6} Sn _{0.4} O ₂	6.8	4.4	0.446	79.1	0.778

N-Ir_{0.6}Sn_{0.4}O₂, respectively, matching well with the HRTEM images. The crystalline size of synthesized Ir–Sn samples were estimated using the Scherrer equation in Table 1. The average sizes calculated from the (1 1 0) and (1 0 1) planes for $x = \text{Ir}_{0.6}\text{Sn}_{0.4}\text{O}_2$ ($x = \text{N}$, S200, S100 and 40) were 4.6, 4.4, 2.3 and 2.3 nm, respectively. The reduced sizes for the TBP-assistant samples (especially for S200- and S100-Ir_{0.6}Sn_{0.4}O₂), to some extent, is due to the TBP protection from crystallization in the calcination process.

XPS spectra of Ir4f and Sn3d were utilized to probe the formation of oxide surfaces in Fig. 4. The Ir4f region in the studied samples exhibited two peaks around 61.7 and 64.7 eV corresponding to the Ir4f7/2 and Ir4f5/2 lines, respectively (Fig. 4(a)). The Ir4f7/2 binding energy is obviously higher than for the metallic Ir (60.9 eV [17]), indicating a higher oxidation level of the iridium species. Furthermore, the asymmetric peaks for Ir4f were observed for all Ir–Sn samples independent of the preparation procedure, originating from the multiple oxidation states [43].

By fitting the Ir4f region and Sn3d, in Table 2, we have found that there was a small shift (ca. 0.2 eV) in the peak positions (Ir4f7/2 61.6–61.8 eV and Sn3d5/2 486.3–486.5). The higher values for the TBP-assistant samples (especially for S100-Ir_{0.6}Sn_{0.4}O₂) could be ascribed to the strengthened Ir–Sn solid-solution phase. The fitted results for the Ir4f2/7 electro-orbit exhibited that three different valence states of the Ir element are present in the various Ir–Sn samples, including Ir³⁺4f7/2 (61.45–61.63 eV), Ir⁴⁺4f7/2 (62.40–62.66 eV) and Ir⁶⁺4f7/2 (63.64–64.01 eV). Based on the surface analysis, the mean valence for the Ir species was between 3.98 and 4.11 in the synthesized samples, consistently with the molecular

formula of IrO₂, and the S40-Ir_{0.6}Sn_{0.4}O₂ sample with the nanorod structure obtained the highest Ir mean valence (4.11). Besides, the Ir/(Ir + Sn) atomic ratio for the each surfactant-assistant materials (especially for S100-Ir_{0.6}Sn_{0.4}O₂) at surface was obviously larger than the bulk value by ICP (see Table 1), indicating the IrO₂-riched surface. Whereas, it was further found that the Ir/(Ir + Sn) surface atomic ratio of N-Ir_{0.6}Sn_{0.4}O₂ was 0.45, which was similar to the bulk value obtained by ICP. The result obtained would be a good proof that the increased SnO₂ sites (especially for N-Ir_{0.6}Sn_{0.4}O₂) were not covered by the active Ir component, resulting in two segregated Ir and Sn phases.

3.2. Half-cell performance

In a subsequent study, the activity and durability of electrocatalysts synthesized with different TBP contents were evaluated by a half-cell method in N₂-purged 0.5 M H₂SO₄. For comparison, the IrO₂ samples, containing N-IrO₂ without TBP and S100-IrO₂ with the molar ratio of Ir/F127 = 100, were prepared using the similar procedure and then evaluated the performance for OER

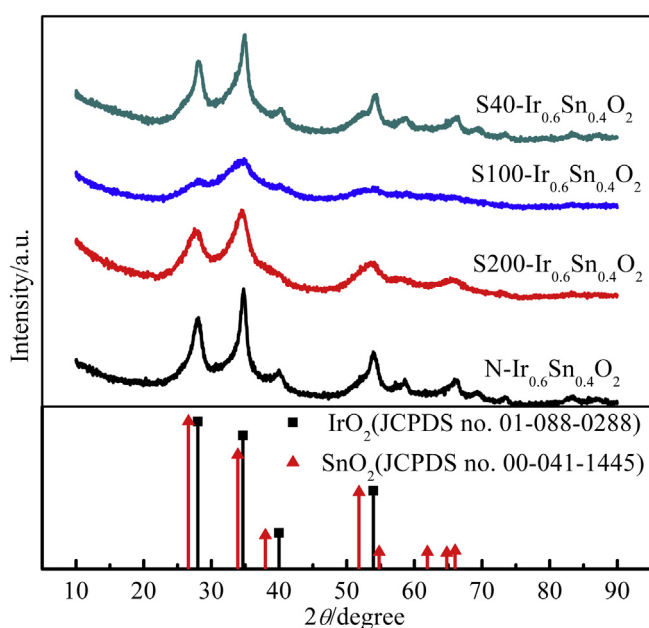


Fig. 3. XRD patterns of the prepared Ir_{0.6}Sn_{0.4}O₂ samples. Stick reference patterns for rutile IrO₂ and SnO₂ are also included.

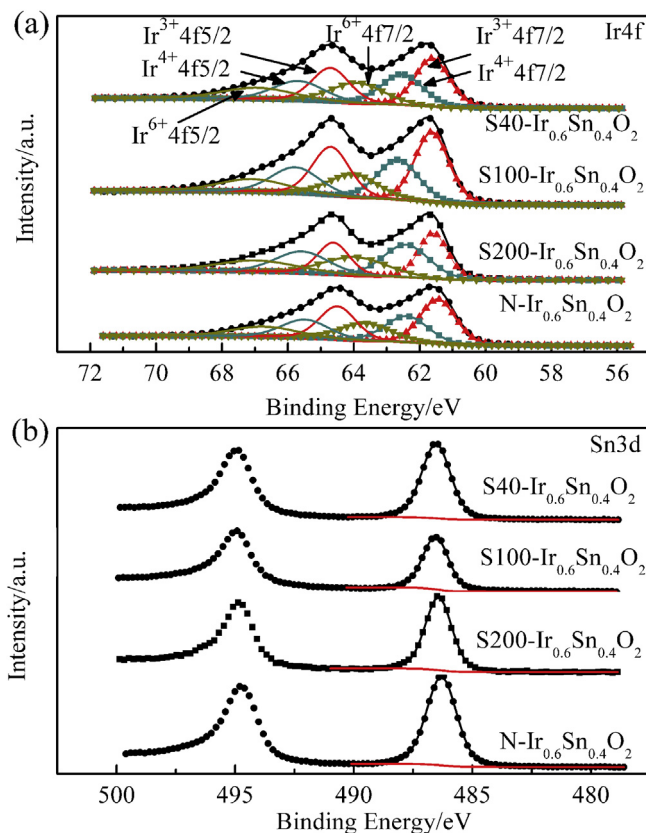


Fig. 4. XPS spectra for (a) Ir4f and (b) Sn3d in the prepared Ir_{0.6}Sn_{0.4}O₂ samples. Solid circle – raw data; (Symbol+) line – fit data. Background lines for Ir4f and Sn3d5/2 are also included.

Table 2
XPS analysis for the prepared $\text{Ir}_{0.6}\text{Sn}_{0.4}\text{O}_2$ samples.

Sample	Ir4f7/2			Ir valence	Sn3d5/2 position (eV)
	Position (eV)	Intensity (%)	Mean position (eV)		
$\text{Ir}_{0.6}\text{Sn}_{0.4}\text{O}_2$	Ir^{3+} (61.45)	44.21	61.61	4.05	Sn^{4+} (486.30)
	Ir^{4+} (62.40)	31.37			
	Ir^{6+} (63.64)	24.42			
S200- $\text{Ir}_{0.6}\text{Sn}_{0.4}\text{O}_2$	Ir^{3+} (61.59)	45.31	61.77	4.01	Sn^{4+} (486.43)
	Ir^{4+} (62.42)	31.66			
	Ir^{6+} (63.96)	23.04			
S100- $\text{Ir}_{0.6}\text{Sn}_{0.4}\text{O}_2$	Ir^{3+} (61.63)	46.09	61.80	3.98	Sn^{4+} (486.52)
	Ir^{4+} (62.66)	31.90			
	Ir^{6+} (64.01)	22.01			
S40- $\text{Ir}_{0.6}\text{Sn}_{0.4}\text{O}_2$	Ir^{3+} (61.61)	41.59	61.75	4.11	Sn^{4+} (486.44)
	Ir^{4+} (62.53)	31.92			
	Ir^{6+} (63.89)	26.49			

using the half-cell system. It is expected that SnO_2 acting primarily to dilute the noble metal oxide could improve the Ir utilization [29].

CV is a surface sensitive technique where each material has a unique spectrum in a given medium. Fig. 5 shows typical CV curves of Ir–Sn oxide electrocatalysts at a scan rate of 50 mV s^{-1} . The CV shapes exhibited the broad waves, resulting from the solid-state redox reactions where the surface active Ir species were oxidized or reduced accompanied by proton exchange between the oxide and the electrolyte [31,44]. The peak located at around $0.65 \text{ V}_{\text{SCE}}$ was consistent with the redox couples $\text{Ir}^{\text{III}}/\text{Ir}^{\text{IV}}$. The $\text{Ir}^{\text{IV}}/\text{Ir}^{\text{VI}}$ peak for S40- $\text{Ir}_{0.6}\text{Sn}_{0.4}\text{O}_2$ at the potential of (ca.) $1.0 \text{ V}_{\text{SCE}}$ was apparently stronger than that for other studied electrocatalysts, ascribing to the higher Ir valence at the particle surface based on the XPS data. When the molar ratio of (Ir + Sn)/F127 was 100, the fabricated electrocatalyst was detected with the largest current density composed of two different contributions, i.e. faradic current and double-layer capacitance. It means that S100- $\text{Ir}_{0.6}\text{Sn}_{0.4}\text{O}_2$ would obtain the enhanced surface active areas/sites and thus the highest activity for OER [12,14,29,45,46], and the improved Ir-utilization because of the low-cost Sn addition in contrast with S100- IrO_2 . At the same time, the decreased current density of S200- and 40- $\text{Ir}_{0.6}\text{Sn}_{0.4}\text{O}_2$ was originated from the increased exposed SnO_2 sites at nanomaterial surface. In particular, the current density values of N- $\text{Ir}_{0.6}\text{Sn}_{0.4}\text{O}_2$ and N- IrO_2 in the scanning potential window were

much less than those of other materials prepared using TBP, which could be explained by the low total pore volume and poor electro conduction with the high Sn-content surface. Therefore, the obvious difference of CV curves among the prepared Ir–Sn samples clearly demonstrated that TBP with the different contents can efficiently controlled the synthesis of IrO_2 – SnO_2 NPs.

The ratio of anodic-charge/cathodic-charge (Q_a/Q_c) was often used to examine the reversibility of redox and charging process [29], which was obtained by calculating the CV charges between 0.15 and $1.15 \text{ V}_{\text{SCE}}$ of the forward and backward sweep according to Eq. (2). As shown in Fig. 6, the Q_a/Q_c ratios for the F127 samples (especially for S200- and S100- $\text{Ir}_{0.6}\text{Sn}_{0.4}\text{O}_2$) were very close to 1.0, which confirmed the excellent reversible behavior in the test system. However, the ratios were over 1.15 for N- $\text{Ir}_{0.6}\text{Sn}_{0.4}\text{O}_2$ with low total pore volume at the above 5 mV s^{-1} of scan rate, resulting from the marked diffusion limitation for the cathodic process and slow transfer of electrons between redox sites in the dispersed oxide material. Since diffusion limitation during the positive sweep arises only at a higher scan-rate, the anodic peak current densities under the fast sweep-rate conditions are generally much larger [44]. As a possible result of the diffusion limitation, the Q_a/Q_c value of over 1.0 for N- IrO_2 was also clearly observed at a higher scan rate. The irreversible behavior thus would provide a reasonable proof that some form of inhibition (related to the limitation of mass diffusion and poor electro conduction within the surface layer) was involved in N- $\text{Ir}_{0.6}\text{Sn}_{0.4}\text{O}_2$ due to the low pore volume and Sn-riched surface.

The catalytic properties for OER can be evaluated by comparing the double-layer capacitance of electrocatalysts which is proportional to the number of surface active sites [12,14,29,45,46] and calculated from CV curves between 0.15 and $1.15 \text{ V}_{\text{SCE}}$. Fig. 7a gives the CV capacitances of the various prepared Ir and Ir–Sn samples. It indicated that the order of voltammetric charges in the studied scan-rate window was: S100- $\text{Ir}_{0.6}\text{Sn}_{0.4}\text{O}_2 > \text{S200-}\text{Ir}_{0.6}\text{Sn}_{0.4}\text{O}_2 > \text{S100-}\text{IrO}_2 \geq \text{S40-}\text{Ir}_{0.6}\text{Sn}_{0.4}\text{O}_2 >> \text{N-}\text{IrO}_2 >> \text{N-}\text{Ir}_{0.6}\text{Sn}_{0.4}\text{O}_2$. The resulting phenomena revealed that the Ir-based electrocatalysts with the significantly enhanced activity and Ir effective utilization could be produced by the Sn addition and the soft-template F127 utilization. Furthermore, the total charge (Q_t) and outer charge (Q_o) were calculated according to Eq. (2) at the scan rates of 2 and 300 mV s^{-1} , respectively. Generally, Q_o always involves the outer active area/site and accessible region for proton penetration, and directly correlates with the OER activity. The largest Q_o value in the prepared catalysts was more than $5000 \text{ mC cm}^{-2} \text{ mg}_{\text{Ir}}^{-1}$ obtained from S100- $\text{Ir}_{0.4}\text{Sn}_{0.6}\text{O}_2$,

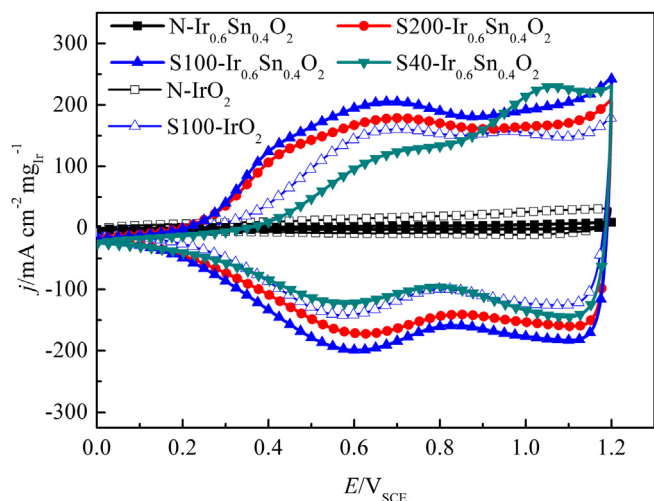


Fig. 5. CV curves of the prepared $\text{Ir}_{0.6}\text{Sn}_{0.4}\text{O}_2$ and IrO_2 samples at 50 mV s^{-1} in $0.5 \text{ M H}_2\text{SO}_4$ at room temperature.

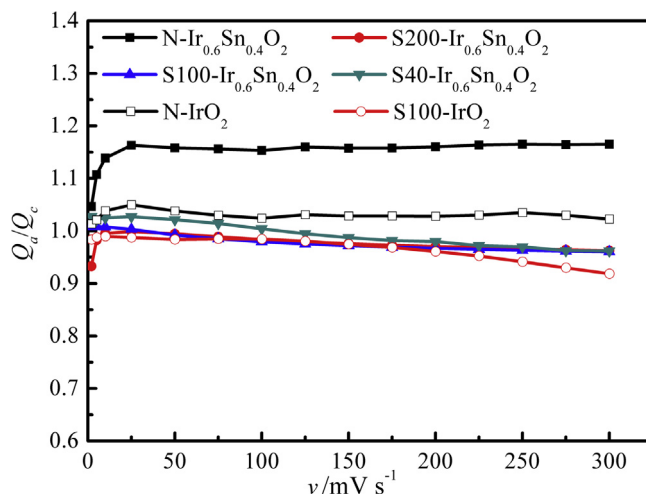


Fig. 6. The reversibility of the pseudo-capacitance process of the prepared $\text{Ir}_{0.6}\text{Sn}_{0.4}\text{O}_2$ and IrO_2 samples.

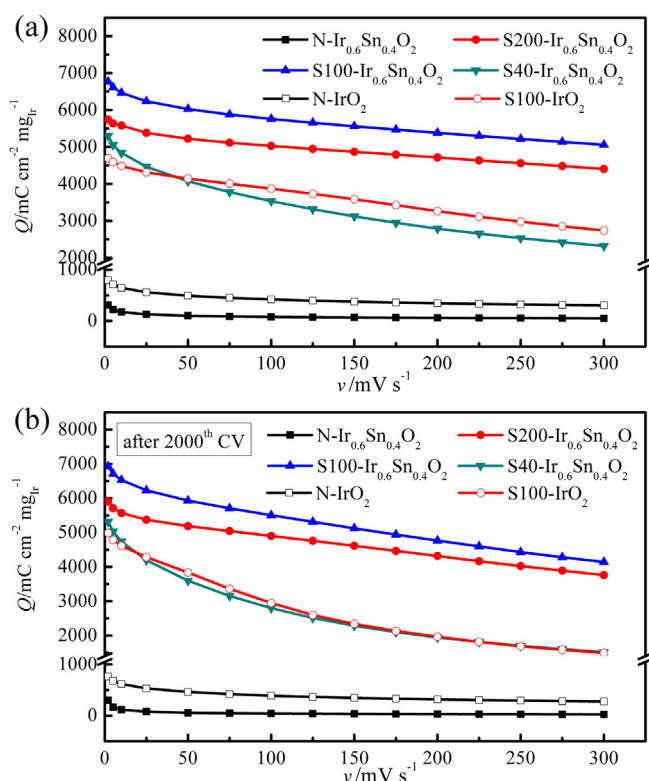


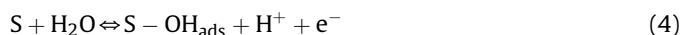
Fig. 7. Dependence of voltammetric charges of the prepared $\text{Ir}_{0.6}\text{Sn}_{0.4}\text{O}_2$ and IrO_2 samples on scan rates in 0.5 M H_2SO_4 (a) before and (b) after the 2000th CV tests at 100 mV s^{-1} .

which was near 100 and 60 times higher than that of $\text{Ir}_{0.6}\text{Sn}_{0.4}\text{O}_2$ and IrO_2 fabricated without TBP, respectively. It is interesting to note that the value was favorably compared to the performances of other IrO_2 -based materials tested under the similar conditions [12,28,31,45,47,48]. Because of the slow diffusion of proton beneath the surface via the inner and less accessible active regions, such as pore, crevices, cracks and grain boundaries, the Q_t value obtained was always larger than Q_o in each studied sample. Meanwhile, the Q_o/Q_t ratio expresses the accessible porosity for the proton beneath in the outer surface and the Ir dispersion for $\text{IrO}_2/\text{SnO}_2$ [12,45,49]. The Q_o/Q_t values were 23.2%, 76.7%, 74.7%, 43.8%, 38.3% and 58.3% for $x\text{-Ir}_{0.4}\text{Sn}_{0.6}\text{O}_2$ ($x = \text{N}, \text{S200}, \text{S100}$ and S40) and $x\text{-IrO}_2$ ($x = \text{N}$ and S100), respectively, demonstrating the improved porous structure and effective Ir utilization at the surface by the proper F127 content.

Fig. 7b shows the voltammetric charges as a function of scan rate after 2000 cycles between 0 and $1.2 \text{ V}_{\text{SCE}}$. Compared with inner charges, the main charges losses presented in the outer, suggesting the changes in surface, i.e. roughness, geometry, electronic band structure, irreversible aggregation, and/or ensemble of multicomponent catalyst. In particular, it was confirmed that S200- and S100- $\text{Ir}_{0.6}\text{Sn}_{0.4}\text{O}_2$ more durably afforded two thousands CV trails than other studied samples, which was mainly related to the enrichment of the steady Ir species, the strengthened Ir–Sn solid-solution structure at the NP surface. It is also important to note that the Sn addition and relatively larger particle size, to some extent, may stabilize the Ir-based catalysts in the acid medium reported by Du and coworkers [50]. On the other hand, our results suggested that N- $\text{Ir}_{0.6}\text{Sn}_{0.4}\text{O}_2$ with irreversible behavior obviously lost its outer charges after the 2000th CV. It is also worthy to mention that the poor stability of most IrO_2 -based electrocatalysts against corrosion is normally associated with insufficient electrical conduction [30,51,52].

The performance of the prepared electrocatalysts toward OER was further examined by conducting LSV at a scan rate of 2 mV s^{-1} . As shown in Fig. 8a, the TBP content for the home-made catalysts showed a strong influence on the OER activity. The poor OER activity was still verified for N- $\text{Ir}_{0.6}\text{Sn}_{0.4}\text{O}_2$, corresponding well with the above CV results. The largest current density in the studied samples was obtained with S100- $\text{Ir}_{0.6}\text{Sn}_{0.4}\text{O}_2$ and S100- IrO_2 at the applied potential window, indicating the highest catalytic activity for OER. The improved performance could be ascribed to the amorphous structure, decreased crystalline size, IrO_2 -rich surface, more outer active sites, higher accessible porosity, etc. Furthermore, the noble-metal loading in the S100- $\text{Ir}_{0.6}\text{Sn}_{0.4}\text{O}_2$ electrode reduced by 40.2% compared with that in the S100- IrO_2 electrode.

The corresponding Tafel plots from the fits of LSV curves are given in Fig. 8b. In our study, a range of OER current density with less than 50 mA cm^{-2} was chosen to obtain the kinetic-controlled Tafel slope, because the current density is low enough that ohmic overpotential and bubble effect can be assumed negligible [53]. Similar Tafel slope was obtained from all the Ir-based samples despite the different metal components and the TBP contents, which revealed the same reaction mechanism. At the relatively lower current density, a range of Tafel slopes from 52 to 73 mV dec^{-1} illustrated that the second step of the Krusil'shchikov Path mechanism [54] is the rate-determining step, by the following Eq. (3) where S denotes an active site. In contrast, the oxygen evolution at the high current density showed a much higher Tafel slope ($115\text{--}144 \text{ mV dec}^{-1}$), suggesting the changes of the rate-determining step and the adsorption contribution of intermediates (possibly related to Eqs. (4) and/or (5)). Particularly, the lowest Tafel slopes at the same potential region were found in S100- $\text{Ir}_{0.6}\text{Sn}_{0.4}\text{O}_2$ and S100- IrO_2 mainly resulting from the lowest overpotential toward oxygen evolution.



After the 2000th CV at 100 mV s^{-1} , in Fig. 8c, active degradation of S200- and S100- $\text{Ir}_{0.6}\text{Sn}_{0.4}\text{O}_2$ detected with the similar durability of S100- IrO_2 were less than the other two Ir–Sn samples and N- IrO_2 , confirming the strongly continuous Ir and Sn phases. Besides, the LSV result also indicated that N- $\text{Ir}_{0.6}\text{Sn}_{0.4}\text{O}_2$ underwent much activate losses during the repetitive CV sweep, which was in accordance with the results of a significant decrease in outer active sites.

3.3. PEMWE cells performance

3.3.1. EIS analysis

The performance of the in-house Ir–Sn oxides was tested for OER in a single PEMWE cell. The EIS measurement can provide available in-situ information of the electrolyzer under the real electrolysis conditions [11,12,45]. The typical EIS spectra were obtained at 1.45 V corresponding to the OER voltage as shown in Fig. 9. Real impedances were observed at low frequencies, indicating no mass transport limitation in the assembled cells. The equivalent circuit was simulated by $LR_{\Omega}(R_1 Q_1)(R_{ct} Q_{dl})$, where L , R_{Ω} , R_{ct} and Q_{dl} are inductor, ohmic resistance, charge transfer resistance and double layer capacitance, respectively. A constant phase element (CPE) is frequently employed to instead of a pure capacitor (Q) to compensate for non-homogeneity, e.g. a rough or porous surface. Hence, a capacitor is often described as follows:

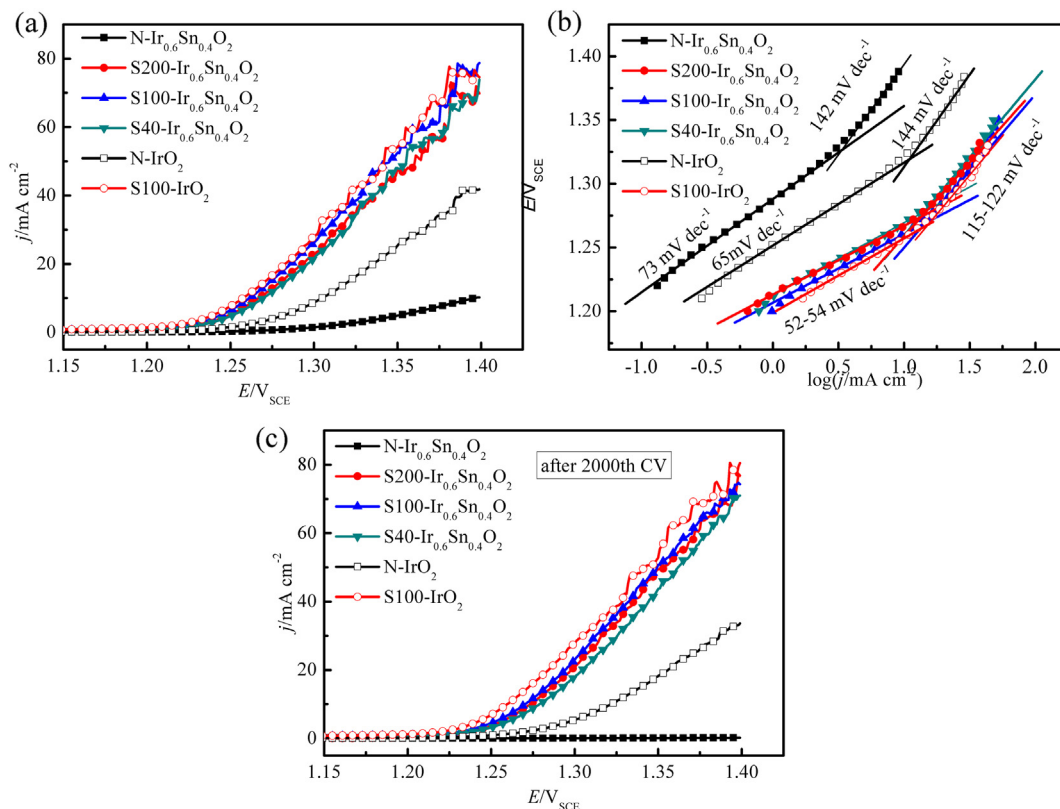


Fig. 8. (a) LSV curves of the prepared Ir_{0.6}Sn_{0.4}O₂ and IrO₂ samples at 2 mV s⁻¹ in 0.5 M H₂SO₄, and (b) Tafel plots (data extracted from LSV measurements) for OER, and (c) LSV curves after the 2000th CV test.

$$Q = \frac{1}{Y_o(iw)^n} \quad (6)$$

where Y_o is a frequency independent constant, w is the angular frequency of the AC signal, i = square root (-1) and n is a factor between 0 and 1. The $R_1 Q_1$ circuit has been attributed to various phenomena, e.g. the diffusion of protons along the oxide grains and the diffusion of reduced oxide sites [11,45,47].

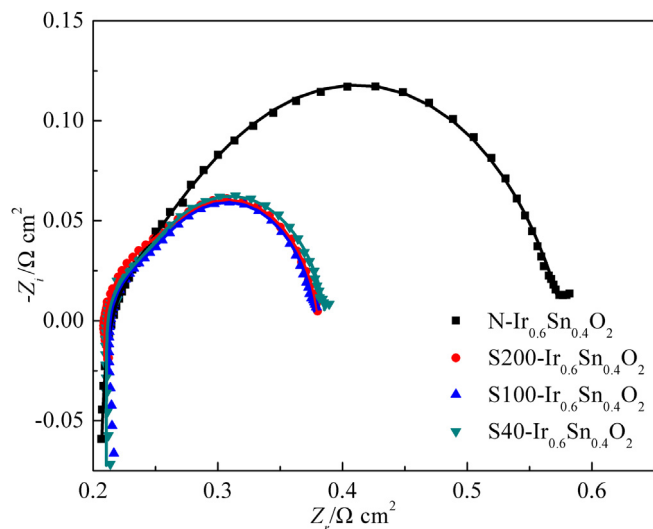


Fig. 9. Impedance spectra for the PEMWE cells at 1.45 V in a sweeping frequency range from 0.1 Hz to 10 kHz, and with an alternate signal of 10 mV. Point – raw data; line – fit data.

As shown in Fig. 9, the simulating results (listed in Table 3) were matched perfectly with the resulting impedance diagrams. The simulating chi-square (χ^2) was around 10^{-4} , presenting credible results. Considering the different cell compactness and fitting deviation, we believe that the slight changes of R_Ω values for each cell were not originated from the varying OER catalysts. It was well known that the cell R_Ω value (ca. $0.2 \Omega \text{ cm}^2$) could be further decreased by applying carbon-material diffusion layer in the anode and a thinner PEM (such as Nafion® 212/1035 membrane) but the cell could not usually maintain a long-term steady running [12,45,47,55]. The R_{ct} value of the N-Ir_{0.6}Sn_{0.4}O₂ cell was almost double of the TBP-catalyst cells, affirming the decreased catalytic activity for N-Ir_{0.6}Sn_{0.4}O₂. Based on the fitting results of Q_{dl} and Q_1 , it is suggested that the circuit elements were not pure capacitors for heterogeneities and rough surfaces in electrodes.

3.3.2. Polarization performance

Fig. 10 gives the steady state polarization curves for PEM cells employing Nafion® 115 membrane as the electrolyte at 80 °C. It showed that the onset voltage was less than 1.4 V for all the Ir–Sn based cells. In contrast to the N-Ir_{0.6}Sn_{0.4}O₂ cell, the cell performance observed was significantly improved by using the Sx-Ir_{0.6}Sn_{0.4}O₂ ($x = 200, 100$ or 40) electrocatalyst. More precisely, low cell voltages with respect to S100-Ir_{0.6}Sn_{0.4}O₂ were 1.631 V at 1000 mA cm^{-2} , and 1.820 V at 2000 mA cm^{-2} , which were about 0.1 and 0.2 V less than those of the N-Ir_{0.6}Sn_{0.4}O₂ cell, respectively. The IR-free voltages in the S100-Ir_{0.6}Sn_{0.4}O₂ cell, by subtracting the ohmic losses from the applied potential, were near the onset oxygen evolution based on EIS results in the investigated current density, e.g. its IR-free voltage was 1.418 V at 1000 mA cm^{-2} . In the published reports, one of the best results found was about 1.60 V at

Table 3

Impedence fitting parameters of the PEMWE cells.

Cell	χ^2 (E ⁻⁴)	L (E ⁻⁷ H)	R_0 (Ω cm ²)	R_1 (Ω cm ²)	Q_1		R_{ct} (Ω cm ²)	Q_{dl}	
					Y_0 (F cm ⁻² s ⁿ⁻¹)	n		Y_0 (F cm ⁻² s ⁿ⁻¹)	n
N-Ir _{0.6} Sn _{0.4} O ₂	7.86	2.10	0.200	0.114	0.355	0.514	0.265	0.117	0.822
S200-Ir _{0.6} Sn _{0.4} O ₂	1.91	0.63	0.209	0.0482	0.210	0.873	0.122	0.492	0.916
S100-Ir _{0.6} Sn _{0.4} O ₂	0.95	2.13	0.213	0.0324	0.203	0.860	0.129	0.465	0.90
S40-Ir _{0.6} Sn _{0.4} O ₂	1.8	2.32	0.210	0.0336	0.211	0.855	0.143	0.214	0.878

1000 mA cm⁻² and 80 °C in the IrO₂-based cell using Nafion® 212 membrane and carbon cloth diffusion layers, and the corresponding IR-free voltage was 1.45 V [12]. Another considerable success on the TBP-assistant electrocatalysts was only 0.77 mg cm⁻² of the noble-metal Ir loading in the anode. Whereas, most published literature were found with 1.2–2 mg cm⁻² Ir loading in the Ir-based PEMWE cell [12,19,21–23,31,56–58]. Therefore, the present results illustrated that the optimum TBP-assistant Ir–Sn catalyst can remarkably reduce energy consumption and cost for the H₂/O₂ production.

4. Conclusions

In this paper, Ir–Sn oxide electrocatalysts with the same ratio of Ir/Sn (3/2) in feed were prepared by an advanced and effective F127-assistant approach. According to complementary physico-chemical methods, the collective data affirmed that the Ir–Sn oxides properties, including morphology (grain-to-rod transition), porosity and oxide state in surface, were efficiently controlled with the varying soft-material (TBP F127) contents. Combining with the half-cell and electrolyzer results, it confirmed that the optimum ratio of (Ir + Sn)/F127 was 100 for the Ir_{0.6}Sn_{0.4}O₂ preparation. The synthesized S100-Ir_{0.6}Sn_{0.4}O₂ presented the obviously improved activity, sufficient stability and correspondingly high Ir utilization under the OER conditions, owing to the amorphous structure, decreased crystalline size, solid-solution state and IrO₂-rich at the surface, enhanced outer active areas/sites and high accessible porosity.

In the S100-Ir_{0.6}Sn_{0.4}O₂ cell, the cell voltages with Nafion® 115 membrane and a Ti-material anode diffusion layer at 80 °C were 1.631 V at 1000 mA cm⁻² and 1.82 V at 2000 mA cm⁻², equating to thermodynamic energy efficiencies of 90.7% and 81.3%,

respectively. Meanwhile, its IR-free voltage in the tested current density range was much closer to the onset oxygen evolution voltage which was less than 1.4 V. Furthermore, the successful example only utilized about 0.77 mg cm⁻² of the precious-metal Ir loading at the oxygen-evolution side due to a high Ir utilization. Hence, it is clear that the Ir–Sn OER catalyst fabricated by the modified TBP route makes it possible to meet all of the requirements of material improvements toward OER, containing high electrocatalytic activity, superior durability and low cost.

Acknowledgments

We are grateful to the Natural Science Foundation of China (20936008 and 21176234).

References

- [1] M.A. Rosen, D.S. Scott, *Int. J. Hydrogen Energy* 23 (1998) 653–659.
- [2] F. Barbir, *Sol. Energy* 78 (2005) 661–669.
- [3] S. Srinivasan, F.J. Salzano, *Int. J. Hydrogen Energy* 2 (1977) 53–59.
- [4] R.N. Singh, J.P. Singh, B. Lal, M.J.K. Thomas, S. Bera, *Electrochim. Acta* 51 (2006) 5515–5523.
- [5] S. Sharma, N. Garg, K.V. Ramanujachary, S.E. Lofland, A.K. Ganguli, *Cryst. Growth Des.* 12 (2012) 4202–4210.
- [6] Y.J. Leng, G. Chen, A.J. Mendoza, T.B. Tighe, M.A. Hickner, C.Y. Wang, *J. Am. Chem. Soc.* 134 (2012) 9054–9057.
- [7] B. Cui, H. Lin, J.B. Li, X. Li, J. Yang, J. Tao, *Adv. Funct. Mater.* 18 (2008) 1440–1447.
- [8] X. Wu, K. Scott, *J. Power Sources* 206 (2012) 14–19.
- [9] S. Park, Y.Y. Shao, J. Liu, Y. Wang, *Energy Environ. Sci.* 5 (2012) 9331–9344.
- [10] T. Reier, M. Oezaslan, P. Strasser, *ACS Catal.* 2 (2012) 1765–1772.
- [11] E. Rastan, G. Hagen, R. Tunold, *Electrochim. Acta* 48 (2003) 3945–3952.
- [12] J.Y. Xu, G.Y. Liu, J.L. Li, X.D. Wang, *Electrochim. Acta* 59 (2012) 105–112.
- [13] L.E. Owe, M. Tsyppkin, K.S. Wallwork, R.G. Haverkamp, S. Sunde, *Electrochim. Acta* 70 (2012) 158–164.
- [14] W. Hu, Y.Q. Wang, X.H. Hu, Y.Q. Zhou, S.L. Chen, *J. Mater. Chem.* 22 (2012) 6010–6016.
- [15] X. Wu, K. Scott, *Int. J. Hydrogen Energy* 36 (2011) 5806–5810.
- [16] X. Wu, J. Tayal, S. Basu, K. Scott, *Int. J. Hydrogen Energy* 36 (2011) 14796–14804.
- [17] W.H. Lee, H. Kim, *Catal. Commun.* 12 (2011) 408–411.
- [18] J.C. Cruz, V. Baglio, S. Siracusano, R. Ornelas, L. Ortiz-Frade, L.G. Arriaga, V. Antonucci, A.S. Arico, *J. Nanopart. Res.* 13 (2011) 1639–1646.
- [19] S.D. Song, H.M. Zhang, X.P. Ma, Z.G. Shao, R.T. Baker, B.L. Yi, *Int. J. Hydrogen Energy* 33 (2008) 4955–4961.
- [20] E. Ortel, T. Reier, P. Strasser, R. Kraehnert, *Chem. Mater.* 23 (2011) 3201–3209.
- [21] G.F. Li, H.M. Yu, W. Song, M.L. Dou, Y.K. Li, Z.G. Shao, B.L. Yi, *ChemSusChem* 5 (2012) 858–861.
- [22] F.M. Sapountzi, S.C. Divane, E.I. Papaioannou, S. Souentie, C.G. Vayenas, *J. Electroanal. Chem.* 662 (2011) 116–122.
- [23] S. Siracusano, V. Baglio, A. Stassi, R. Ornelas, V. Antonucci, A.S. Arico, *Int. J. Hydrogen Energy* 36 (2011) 7822–7831.
- [24] K. Kadakia, M.K. Datta, P.H. Jampani, S.K. Park, P.N. Kumta, *J. Power Sources* 222 (2013) 313–317.
- [25] R.X. Sun, H.B. Xu, N.F. Wan, J. Wang, *Chem. J. Chin. Univ.* 28 (2007) 904–908.
- [26] P. Mazur, J. Polonsky, M. Paidar, K. Bouzek, *Int. J. Hydrogen Energy* 37 (2012) 12081–12088.
- [27] J. Polonský, I.M. Petrushina, E. Christensen, K. Bouzek, C.B. Prag, J.E.T. Andersen, N.J. Bjerrum, *Int. J. Hydrogen Energy* 37 (2012) 2173–2181.
- [28] A. Marshall, M. Tsyppkin, B. Borresen, G. Hagen, R. Tunold, *J. New Mater. Electrochem. Syst.* 7 (2004) 197–204.
- [29] A. Marshall, B. Borresen, G. Hagen, M. Tsyppkin, R. Tunold, *Electrochim. Acta* 51 (2006) 3161–3167.
- [30] G.H. Chen, X.M. Chen, P.L. Yue, *J. Phys. Chem. B* 106 (2002) 4364–4369.
- [31] A.T. Marshall, R.G. Haverkamp, *Electrochim. Acta* 55 (2010) 1978–1984.

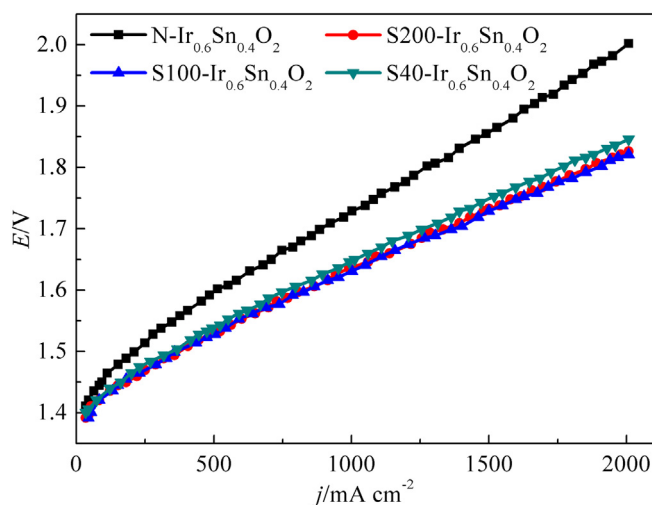


Fig. 10. Steady state polarization curves of the PEMWE cells using Nafion® 115 membrane and the prepared Ir_{0.6}Sn_{0.4}O₂ samples as anode catalyst at 80 °C.

- [32] A. Di Blasi, C. D'Urso, V. Baglio, V. Antonucci, A.S. Arico, R. Ornelas, F. Matteucci, G. Orozco, D. Beltran, Y. Meas, L.G. Arriaga, J. Appl. Electrochem. 39 (2009) 191–196.
- [33] G. Li, H. Yu, W. Song, X. Wang, Y. Li, Z. Shao, B. Yi, Int. J. Hydrogen Energy 37 (2012) 16786–16794.
- [34] P. Alexandridis, Chem. Eng. Technol. 34 (2011) 15–28.
- [35] P. Alexandridis, M. Tsianou, Eur. Polym. J. 47 (2011) 569–583.
- [36] E. Ramasamy, C. Jo, A. Anthonysamy, I. Jeong, J.K. Kim, J. Lee, Chem. Mater. 24 (2012) 1575–1582.
- [37] N. Dahal, I.A. Ibarra, S.M. Humphrey, J. Mater. Chem. 22 (2012) 12675–12681.
- [38] P. Khullar, A. Mahal, V. Singh, T.S. Banipal, G. Kaur, M.S. Bakshi, Langmuir 26 (2010) 11363–11371.
- [39] S. Ardizzzone, C.L. Bianchi, L. Borgese, G. Cappelletti, C. Locatelli, A. Minguzzi, S. Rondinini, A. Vertova, P.C. Ricci, C. Cannas, A. Musinu, J. Appl. Electrochem. 39 (2009) 2093–2105.
- [40] X. Yan, H. Liu, K.Y. Liew, J. Mater. Chem. 11 (2001) 3387–3391.
- [41] G. Landazuri, V.V.A. Fernandez, J.F.A. Soltero, Y. Rharbi, J. Phys. Chem. B 116 (2012) 11720–11727.
- [42] E. Tsuji, A. Imanishi, K. Fukui, Y. Nakato, Electrochim. Acta 56 (2011) 2009–2016.
- [43] G.K. Wertheim, H.J. Guggenheim, Phys. Rev. B 22 (1980) 4680–4683.
- [44] L.D. Burke, D.P. Whelan, J. Electroanal. Chem. Interfacial Electrochem. 162 (1984) 121–141.
- [45] J.B. Cheng, H.M. Zhang, G.B. Chen, Y.N. Zhang, Electrochim. Acta 54 (2009) 6250–6256.
- [46] S. Ardizzzone, G. Fregonara, S. Trasatti, Electrochim. Acta 35 (1990) 263–267.
- [47] J.B. Cheng, H.M. Zhang, H.P. Ma, H.X. Zhong, Y. Zou, Int. J. Hydrogen Energy 34 (2009) 6609–6624.
- [48] Q.F. Wang, F.M. Wu, N. Wang, L. Wang, X.W. Zhang, Electrochim. Acta 74 (2012) 227–234.
- [49] J. Gaudet, A.C. Tavares, S. Trasatti, D. Guay, Chem. Mater. 17 (2005) 1570–1579.
- [50] W. Du, Q. Wang, D. Saxner, N.A. Deskins, D. Su, J.E. Krzanowski, A.I. Frenkel, X. Teng, J. Am. Chem. Soc. 133 (2011) 15172–15183.
- [51] M. Carmo, D.L. Fritz, J. Mergel, D. Stolten, Int. J. Hydrogen Energy 38 (2013) 4901–4934.
- [52] A. de Oliveira-Sousa, M.A.S. da Silva, S.A.S. Machado, L.A. Avaca, P. de Lima-Neto, Electrochim. Acta 45 (2000) 4467–4473.
- [53] C.M. Hwang, M. Ishida, H. Ito, T. Maeda, A. Nakano, Y. Hasegawa, N. Yokoi, A. Kato, T. Yoshida, Int. J. Hydrogen Energy 36 (2011) 1740–1753.
- [54] Y. Matsumoto, E. Sato, Mater. Chem. Phys. 14 (1986) 397–426.
- [55] H.N. Su, B.J. Bladergroen, S. Pasupathi, V. Linkov, S. Ji, Int. J. Electrochem. Sci. 7 (2012) 4223–4234.
- [56] L.R. Ma, S. Sui, Y.C. Zhai, Int. J. Hydrogen Energy 34 (2009) 678–684.
- [57] J.Y. Xu, M. Wang, G.Y. Liu, J.L. Li, X.D. Wang, Electrochim. Acta 56 (2011) 10223–10230.
- [58] P. Millet, N. Mbemba, S.A. Grigoriev, V.N. Fateev, A. Aukauloo, C. Etiévant, Int. J. Hydrogen Energy 36 (2011) 4134–4142.